Aerospace Science and Technology 165 (2025) 110475

Contents lists available at ScienceDirect

Aerospace Science and Technology

journal homepage: www.elsevier.com/locate/aescte

Original article

Experimental investigation of vortex ring state in an eVTOL propeller

Alberto Savino [a], Andrea Gianotti [a], Giovanni Droandi [b], Mike Kerho [b], Alex Zanotti [a,*]

[a] Politecnico di Milano, Dipartimento di Scienze e Tecnologie Aerospaziali, via La Masa 34, 20156, Milan, Italy
[b] Archer Aviation, San Jose, CA, USA

ARTICLE INFO

Communicated by George N. Barokas

Keywords:
Aerodynamics
Wind tunnel
Particle image velocimetry
Vortex ring state
eVTOL

ABSTRACT

This study presents an experimental investigation of the vortex ring state condition occurring in vertical descent of an eVTOL aircraft propeller. Wind tunnel tests were conducted on a propeller model representative of the tilter propeller of the Archer Maker eVTOL aircraft in 1:4 scale. The study focused on the characterization of the propeller aerodynamic performance and flow physics during descent flight conditions. With this aim, thrust and torque measurements along with Particle Image Velocimetry surveys were performed during the wind tunnel campaign reproducing both axial flight and a 10° propeller tilt angle. Multiple descent rate conditions were reproduced and analyzed with the propeller operating at different rotational speeds. Test results highlighted a significant decrease in performance during vortex ring state, occurring consistently at the same descent ratio along with the tested rotational speeds. Flow field surveys clearly reveal the topology of vortex ring generation as function of the descent ratio, allowing for a quantitative characterization of vortex ring dimensions and wandering.

1. Introduction

One of the most promising innovations aiming to revolutionize aviation in the coming years are eVTOLs, Vertical Take-Off and Landing aircraft powered by electric propulsion. Leveraging the coordinated operation of multiple propellers, eVTOLs can easily transition from forward to vertical flight, vectoring the generated thrust. As a result, eVTOLs can operate effectively without need for runways, making them suitable for short-range flight over metropolitan areas. This new aircraft concept promises to revolutionize urban mobility. Indeed, positioning as a new short-range air transport, they will be able to replace ground vehicles with direct routes, avoiding traffic and cutting commute time.

A crucial aspect in the adoption of a new air transport aircraft within urban mobility concerns safety. One of the most critical aerodynamic conditions concerning safety for rotorcraft occurs during the vertical descent phase, i.e. vortex ring state (VRS). VRS is an aerodynamic condition that occurs when a rotor or propeller descends into its own wake, causing the airflow to recirculate around the rotor disk in the form of a vortex ring. This leads to a significant loss of thrust, generally resulting in reduced control and performance. When the aircraft is descending at low descent rates such that the velocity of the propeller-induced flow is higher than the descent speed, the wake is convected away from the propeller disk, forming a clean slipstream between the induced flow and the surrounding air. When the descent speed is comparable to the speed of the propeller-induced flow, the propeller wake is no longer convected away. Thus, blade tip vortices collect into a large vortex, generating a recirculating flow around the edge of the propeller disk [1,2].

The airflow in VRS condition is highly unsteady, and the interaction between the vortex ring and the propeller blades results in a loss of thrust, loads fluctuations, and vibrations. The reduction of thrust is mainly caused by the downward flow velocity induced by the vortex ring remaining close to propeller disk, while loads fluctuations are due to the high unsteadiness associated to vortex ring generation and shedding. Therefore, the VRS onset could lead to potentially hazardous situations for the aircraft. As the aircraft approaches VRS, it may experience an uncommanded drop in altitude and the pilot may lose control effectiveness along the vertical axis. This behavior has been typically observed in helicopters and tiltrotors. To ensure a safe vertical descent, it is necessary to prevent the aircraft from exceeding vertical and near-vertical speeds that could lead to enter VRS conditions [3]. To date, numerous experimental and numerical investigations have been conducted to study VRS in helicopter and tiltrotor aircraft. These studies, employing a wide variety of different methods, have been extensively documented in the literature by numerous authors.

One of the earliest experimental studies on VRS was conducted by Yaggy and Mort [4]. The authors investigated through extensive wind

* Corresponding author.
E-mail address: Alex.Zanotti@polimi.it (A. Zanotti).

https://doi.org/10.1016/j.ast.2025.110475
Received 21 December 2024; Received in revised form 6 June 2025; Accepted 10 June 2025
Available online 13 June 2025
1270-9638/© 2025 The Author(s). Published by Elsevier Masson SAS. This is an open access article under the CC BY-NC-ND license (http://creativecommons.org/licenses/by-nc-nd/4.0/).

Nomenclature

A_T	propeller thrust spectrum amplitude [N]	$\bar{T}$	mean propeller thrust [N]
A_Q	propeller torque spectrum amplitude [N m]	T_h	propeller thrust in hover [N]
C_T	thrust coefficient $= T/(\rho\pi R^4 n^2)$ [-]	V_∞	freestream speed [m s^{-1}]
C_Q	torque coefficient $= Q/(\rho\pi R^5 n^3)$ [-]	V_i	propeller induced velocity $= \sqrt{T/(2\rho\pi R^2)}$
DR	descent ratio $= V_\infty/v_h$	V_h	propeller induced velocity in hover $= \sqrt{T_h/(2\rho\pi R^2)}$
h	hover flight condition	V_{tip}	blade tip velocity
J	propeller advance ratio $= V_\infty/V_{tip}$	V_θ	tangential velocity
n	rotational speed [rad/s]	V_{θ_v}	maximum tangential velocity at vortex ring radius coordinate
Q	propeller torque [N m]	x	reference axis normal to propeller shaft
$\bar{Q}$	mean propeller torque [N m]	z	reference axis aligned with propeller shaft
r	blade radial coordinate [m]	ρ	freestream air density [kg m^{-3}]
r_v	vortex ring radius [m]	α	propeller tilt angle [°]
R	propeller radius [m]		
T	propeller thrust [N]		

tunnel testing vertical and near-vertical descent states which cause a propeller to experience VRS condition. Experimental results showed that VRS can lead to substantial thrust oscillations on a propeller, in some cases up to 75% of steady-state thrust and characterized by an average oscillation period of 0.2 s. In April 2000, a V-22 Osprey tiltrotor operated by the United States Marine Corps crashed during a night training exercise killing all 19 U.S. Marines on board. During the investigation that followed the crash it was established that moments before the accident the aircraft initiated a descent maneuver dropping altitude at a rate of descent beyond the approved flight envelope. This caused the aircraft to enter into VRS that eventually led it to lose lift and crash to the ground. After the V-22 accident, it became abundantly clear that VRS was only partially understood, and further investigations were necessary in order to gain a more in depth understanding of this complex aerodynamics condition and its effects on helicopters and tiltrotors flight characteristics. In 2001 Betzina [5] conducted an experimental investigation in the NASA Ames 80- by 120-foot wind tunnel test facility using a single V-22 proprotor scaled model (10.5% scale) operating at high descent angles in helicopter mode. During this test campaign, however, the author observed that the image plane used to simulate the dual proprotor configuration of the V-22 had non-negligible effects on the measurements collected, implying that a two-proprotor configuration may have significantly different VRS characteristics than a single proprotor. The author concluded that additional research was necessary in order to determine VRS characteristics for a two-proprotor configuration. In a study published in 2004, Brand et al. [6] documented the main results of a thorough investigation of the V–22's low-speed and high rate of descent flight characteristics. The authors investigated multiple flight regimes through flight testing, defining an operational envelope for the aircraft, demonstrating flight regimes free from VRS, and confirming the ability of the V–22 to recover from the condition. The study focused on the identification of the onset of the VRS conditions at high descent rates, providing valuable data that helped improve safety and operational procedures of the aircraft. Furthermore, experimental results highlighted that the V-22 VRS boundaries were very similar to the ones exhibited by more conventional helicopters, while distinguishing for lateral control asymmetry once an individual tiltrotor entered into VRS that provides a consequent uncommanded roll.

To gain a deeper understanding of VRS and the mechanisms driving it, over the years many researchers have conducted studies exploring both the aerodynamic performance implications and the intricate flow physics associated with this complex phenomenon. For instance, Stack [7] performed an experimental investigation of VRS on a rotor model in a water tunnel to explore the physics of the wake evolution in VRS conditions. Flow visualizations highlighted wake instabilities and the formation and shedding of a thick vortex ring from the merging of single blade tip vortices. Moreover, instantaneous thrust measurements showed low frequency oscillations attributable to vortex ring formation and shedding. Shetty and Selig [8] provided a detailed analysis of how geometric parameters such as blade radius and collective pitch as well as propeller solidity and activity factor affect thrust characteristics of small-scale propellers in VRS condition. Tests revealed that thrust loss and fluctuation amplitudes during VRS condition were highly dependent on blade pitch and propeller geometry, and emphasized the need for optimizing blade design to mitigate its effects.

In addition to experimental work, extensive computational efforts have been dedicated to simulating VRS despite the challenges of modeling such a highly unsteady phenomenon. To cite one of the first numerical studies, Inoue et al. [9] performed 3D unsteady Euler Direct Numerical Simulations aimed to identify and clarify the nature of the vortex ring state and autorotation for a helicopter rotor. Şenipek et al. [10] used a numerical approach based on Viscous Vortex Particle Method (VVPM) to model the descent envelope and predict VRS of a single eVTOL rotor. Numerical simulations were conducted reproducing several descent rates, forward velocities, collective pitch and rotational speeds. As a result, VRS envelopes identified the critical flight conditions in terms of thrust and load oscillations, while flow visualization revealed how the generated vortex ring interacts with the rotor itself and evolves into the wake. Another recent numerical activity was focused on the study of quasi-vortex-ring state for a multi-axis propulsive wing aircraft [11]. This work provided a physical investigation of the change in the flow field structure and wake of the propulsive wing as well as the evolution mechanism of the quasi-VRS. Thus, recovery strategies for the quasi-VRS and windmill–brake state were proposed and analyzed in terms of aerodynamic forces of the propulsive wing.

Despite the extensive research conducted on VRS for helicopters and tiltrotor applications, the study of this phenomenon needs to be re-evaluated in the context of emerging eVTOLs and their propellers. In fact, Shetty and Selig [8] have already shown that blade geometry influences VRS on conventional propeller designs. Key differentiators of eVTOL vehicles, such as distributed electric propulsion and higher disk loading requirements, drive significantly different propeller geometries compared to traditional helicopter and tiltrotor rotors. eVTOL propellers often exhibit highly nonlinear twist and chord distributions, coupled with low aspect ratio blades, resulting in a unique design that diverges from more conventional helicopter rotors. Moreover, eVTOL propeller blades are characterized by a higher structural stiffness than helicopter rotor blades and are generally designed to operate at higher rotational speeds. Differences in eVTOL aircraft architecture and propeller blade design could affect the mechanisms that drive VRS with implications on both vehicle aerodynamic performance and the underlying flow physics. Therefore, a comprehensive experimental characterization of VRS for an eVTOL propeller geometry could provide more detailed insights for a thorough re-evaluation of the phenomenon as well as for the



Fig. 1. Picture of Archer Aviation's Maker eVTOL demonstrator vehicle during a hovering flight test event.

validation of numerical approaches to simulate such a complex flight scenario.

With these aims, the present work describes the results of an experimental activity focused on the characterization of the aerodynamic performance of a eVTOL aircraft propeller in VRS. This study also provides a detailed description of the flow field around the propeller in and outside VRS conditions. The work was conducted under a collaboration between the Department of Aerospace Science and Technology of Politecnico di Milano, Italy, and Archer Aviation, California-based eVTOL company. In particular, a scaled model representative of the *Archer Maker* eVTOL tilter propeller (see Fig. 1) was designed and manufactured to perform a dedicated wind tunnel test campaign. The use of a propeller model representative of one of the most promising eVTOL aircraft configuration under development by a leading company in this sector, represents one of the main novelty of the present study with respect to existing literature. Moreover, the geometry of the blade used in the test campaign is going to be disseminated in the present work to enable a thorough assessment of numerical model capabilities against the simulation of such a complex phenomenon in eVTOL scenario. Thrust and torque measurements were performed under different operating conditions to quantify the impact of VRS on propeller aerodynamic performance in relation to key parameters such as descent speed, propeller rotational speed, and propeller tilt angle. This latter parameter represents a point of novelty with respect to the single rotor studies related to classical helicopter configuration. Moreover, a quantitative analysis of flow physics around the propeller in VRS conditions was performed by means of 2C Particle Image Velocimetry (PIV). In particular, in this framework state-of-the-art PIV technique was used for a quantitative evaluation of all the working states of VRS occurrence in a real eVTOL propeller scenario, including tilting angle conditions. Flow surveys enabled analysis of the topology of vortex ring generation, allowing for a quantitative characterization of vortex ring dimensions and wandering. In conclusion, the research collaboration between Politecnico di Milano and Archer Aviation enabled the assessment of the effects of VRS on an eVTOL representative propeller geometry with respect to key parameters, such as propeller tilt angle and descent rate, and realistic flight conditions typical of an eVTOL aircraft. This study also led to the generation of a comprehensive experimental database specific to a single eVTOL propeller and represents a robust milestone before future re-evaluation of the VRS phenomenon in a more realistic scenario for an eVTOL aircraft, also addressing propeller-propeller or propeller-wing interactions.

2. Experimental set up

The experimental activity was performed at the *S. De Ponte* wind tunnel of Politecnico di Milano. The closed-loop wind tunnel consists of four branches with a rectangular cross-section, featuring an height-to-base ratio of 3:2. The closed test chamber has a cross-section that measures 1 m × 1.5 m and is 3 m long, however the actual section slightly increases along the length to compensate the thickening of the boundary layer on the walls. The convergent section upstream of the test section has contraction ratio equal to 7. A maximum speed of 55 $\mathrm{m\,s^{-1}}$ can be reached in the test chamber, with a turbulence level lower than 0.1% and uniformity flow error below 0.1°.

Table 1
Propeller blade geometrical parameters as function of the non-dimensional radial coordinate r/R.

r/R [-]	chord [m]	twist [deg]	sweep [deg]	dihedral [deg]	Airfoil
0.00	0.032	27.1	-	-	NACA2417
0.33	0.030	13.3	-	-	NACA2415
0.50	0.028	9.1	-	-	NACA2414
0.83	0.021	3.4	-	-	NACA2412
0.90	0.019	2.5	0.0	-0.7	NACA2412
0.94	0.018	1.8	1.5	-12.9	NACA2411
0.98	0.016	1.2	15.0	-41.8	NACA2411
1.00	0.008	0.9	31.2	-50.5	NACA2411

2.1. Propeller model set up

The experimental campaign was performed using a 25% scaled model representative of the tilter propeller of Archer *Maker* eVTOL aircraft. The propeller wind tunnel model, with a radius (R) equal to 0.2 m, consisted of 5 blades, a hub element, and a spinner. Each component was built through rapid prototyping technique using a Selective Laser Sintering 3D printer from a bed of nylon-based powders. The blades were installed on the hub using a two-component epoxy adhesive, held in place by a dedicated fixture during the resin curing process. The complete propeller assembly was then statically balanced using a dedicated propeller balancer to correct for any mass imbalances due to small variations in weight and mass distribution between the different blades. The propeller blade collective pitch was set to be representative of the one used for the aircraft during hover flight. Table 1 shows the geometrical parameters of the propeller blade model, with the collective pitch setting included in the reported twist distribution.

Blade chord, sweep, and dihedral angle distributions are the same ones used for Maker aircraft tilter propeller blades. As the airfoils used to design Maker aircraft blades are Archer proprietary, blade models were printed using airfoil geometries from NACA series that reproduced the best fit with respect to the ones used on the aircraft. This choice was dictated by the desire to allow full reproducibility of propeller geometry, thus enabling the use of the present experimental database for the validation of numerical tools reproducing VRS conditions in eVTOL applications. The maximum discrepancy between the real aircraft blade airfoil coordinates and the selected NACA sections is below 1% of blade sectional characteristics around the entire airfoil contour. For the above reasons, and by taking into account the accuracy of 3D printing technique, the propeller wind tunnel model can be considered an accurate reproduction of the geometry of Archer's eVTOL Maker tilter propeller.

Fig. 2 shows the propeller model mounted on a dedicated propeller test rig installed inside the test section of the S. De Ponte wind tunnel. The test rig comprised of the propeller model, a direct drive electric motor, and a bi-axial load cell installed at the top of the wind tunnel strut. An Q80 Hacker brushless RC motor (max. power of 7 kW) was used to drive the wind tunnel propeller model. The propeller was mounted directly on the electric motor flange through the hub. The propeller rotational speed, rotation direction, and motor braking were remotely regulated by an Electronic Speed Controller (ESC) Jeti Model Spin 300 Pro Opto. The propeller thrust and torque were measured using a FUTEK MBA500 strain gauge based bi-axial load cell (200 in-lb and 200 lbs F.S., non-linearity ± 0.25% R.O., non-repeatability ± 0.05% R.O.). The non-metric side of the load cell was installed on the wind tunnel strut using a stiff metal mounting block. A second mounting block was positioned on the metric side of the load cell to interface the load cell

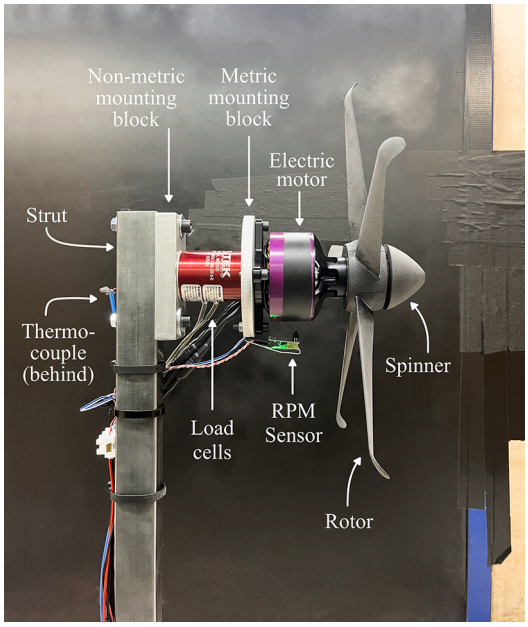


Fig. 2. Picture of the propeller test article installed on a dedicated test rig inside the S. De Ponte wind tunnel test section.

with the propeller system. Load cell signals were acquired by a National Instruments c-DAQ system equipped with strain/bridge NI 9237 modules. Loads signals were sampled at 25 kHz over a 30 s acquisition time window. Each test point was repeated four times and the results were averaged in post-processing. To simulate the required descent conditions in the wind tunnel, the propeller was mounted inverted with respect to the electric motor, so that the airflow induced by the rotation of the blades (V_i) was opposite to the wind tunnel free-stream velocity (V_∞), as shown in the schematic of Fig. 3(a), also illustrating the $x-z$ axes of the propeller-fixed reference system that will be used to present PIV results. Conversely, to simulate climb conditions, the propeller was mounted upright on the electric motor so that the induced velocity (V_i) aligned with the wind tunnel flow (V_∞), as shown in Fig. 3(b).

The model mounted in the wind tunnel was equipped with an optical emitter-sensor to measure propeller rotational speed. A steel strut was used to fix the propeller model to a robust anchor beneath the test section. Wind tunnel tests included configurations with the propeller rotational axis aligned with test section centerline ($\alpha = 0°$) as well as with the propeller disk rotated by an angle $\alpha = 10°$ with respect to the incoming flow (see the propeller tilt angle definition reported in Fig. 3). The latter non-zero propeller tilt angle configuration was reproduced in the wind tunnel by rotating the entire propeller system through a robust joint attached at the base of the supporting strut. Higher propeller tilt angles were not considered during the test, as they could have caused significant interference from the propeller wake impinging on the wind tunnel floor or ceiling. This interference could have introduced systematic errors into the measurements, which would be difficult to quantify and correct.

2.2. PIV set up

The flow field around the propeller blades was surveyed using a two-component (2C) PIV set up. A Quantel Evergreen Nd:Yag double-pulse laser with an output energy of 200 mJ and wavelength of 532 nm was positioned under the plexiglass floor of wind tunnel test section. A 90° optic mirror was used to generate a laser sheet of light to illuminate a plane in the flow field aligned with the longitudinal mid-span plane of the wind tunnel. A double-shutter ILA.PIV.sCMOS camera with a 16 bit 2560×2160 pixels array was mounted on an external metallic structure outside the wind tunnel test section at 90° with respect to laser sheet. The schematic shown in Fig. 4 illustrates the laser sheet and the PIV investigation window with respect to the propeller model positioned in the test section. The dimensions of the investigation window were 400 mm × 338 mm. A particle generator (PIVpart30 by PIVTEC) equipped with Laskin atomizer nozzles was used to seed the wind tunnel test section with 2 μm DEHS particles. Phase-locked PIV measurements were performed at different descent ratios for two different rotational speeds of the propeller. The optical emitter-sensor installed to measure propeller rotational speed was also used to trigger the PIV image acquisition process with a predefined azimuthal position of the master blade used as a reference. Specifically, 300 images pairs were captured for each test condition at a single fixed blade azimuth angle, i.e. with the master blade axis vertically aligned and pointing downward. Phase-locked PIV measurements taken with the master blade fixed at various azimuthal positions did not show any notable differences in the flow field, therefore in the following all PIV measurements are reported and discussed for the case where the master blade axis is vertically aligned and points downward. Image acquisition was performed for a period of 30 s, i.e. at 10 Hz acquisition frequency. Image pair analysis was performed using PIVview 3C software developed by PIVTEC. Post-processing made use of the multi-grid interrogation method [12] starting from a 128 pixels × 128 pixels to a 32 pixels × 32 pixels interrogation window with effective 50% overlap. This methodology results in a spatial resolution between adjacent measurement points of about 2 mm. Based on the pulse-separation time and the optical magnification used for the present measurements, the maximum in-plane velocity error is estimated to be about 0.2 m/s, if considering a conservative error of 0.1 px [13]. A model-fixed reference system with origin positioned at propeller disk center was used to present PIV results (see Fig. 3), where z-axis corresponds to propeller axis of rotation.

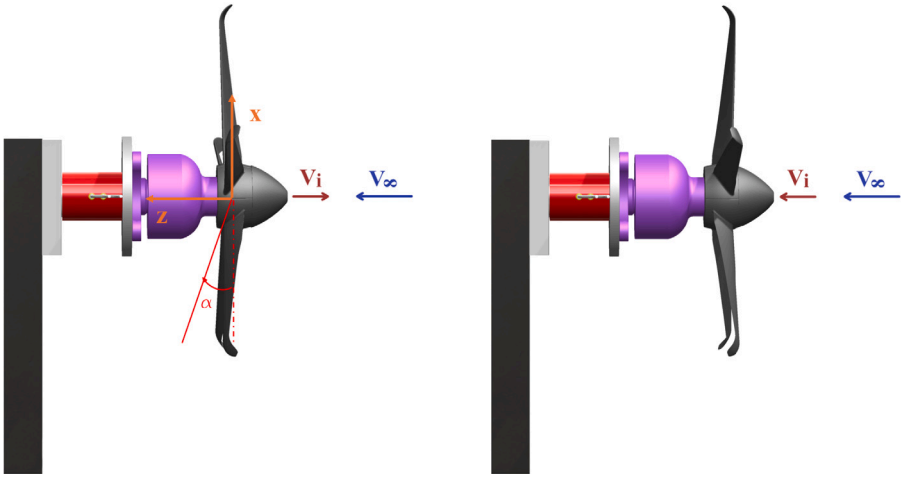
3. Results and discussion

A wide range of climb and descent conditions were tested by running the propeller at a fixed rotational speed while systematically varying the wind tunnel velocity. Two different propeller rotational speed values, 4000 RPM and 5000 RPM, corresponding respectively to Reynolds number equal to $1.22 \cdot 10^5$ and $1.52 \cdot 10^5$ considering the blade chord at 75% span, were considered during the test campaign to assess the effect of propeller rotational speed on VRS onset. The maximum rotational speed was selected to reproduce the highest possible tip Mach number of the blades, while keeping safety during the tests. Similarly, two different propeller disk tilt angles, $\alpha = 0°$ and 10°, were investigated. The wind tunnel velocity was varied from a minimum speed of 5 m s^{-1} to a maximum of 16 m s^{-1} for climb conditions and from a minimum speed of 5 m s^{-1} to a maximum of 10 m s^{-1} for descent cases.

The results of the tests in climb conditions are reported in the following in terms of advance ratio (J), defined as the ratio between the freestream velocity (V_∞) and the propeller tip speed ($R\Omega$). Similarly, the results of the tests in descent conditions are reported in terms of descent ratio (DR), defined as the ratio between the freestream velocity (V_∞) and the induced velocity of the propeller in hover (v_h). Based on the combination of propeller rotational speeds and wind tunnel velocities considered during the test campaign, measurements in climb conditions were performed for a range of advance ratio between 0.048 and 0.191 and in descent conditions for a range of descent ratio between 0.3 and 1.1.

Spinner and motor tares were applied to all runs to remove the effects of spinner and motor, both mounted on the metric side of the load cell and exposed to the freestream during the tests, from the propeller thrust and torque measurements. Tares were generated by installing the spinner element on a 3D printed hub without the propeller blades. Tares were applied in a single step to propeller thrust and torque values by subtracting the spinner and motor measurements from the propeller runs.

Finally, a dedicated test campaign was performed to characterize the aerodynamic performance of the propeller in hover conditions. To



(a) Descent (b) Climb

Fig. 3. Schematic illustrating the propeller installed on the support structure and placed inside the wind tunnel in both descent 3(a) and climb 3(b) configurations. The induced velocity vector and the wind tunnel free-stream vector are also shown for both configurations.

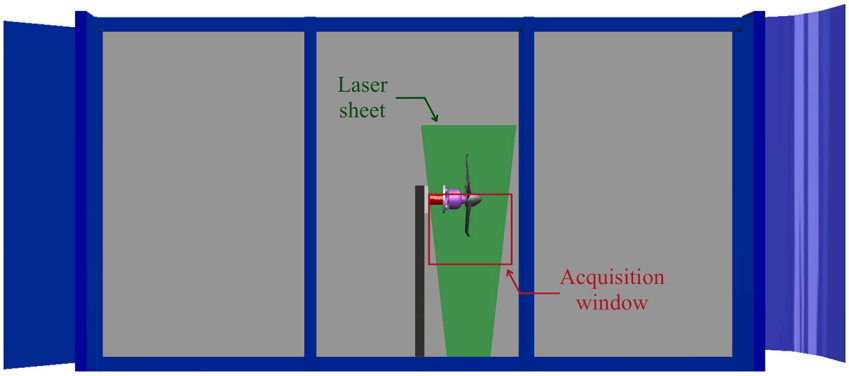


Fig. 4. Schematic of the 2C PIV test setup in the wind tunnel test section.

avoid wall interference and other wind tunnel induced effects, hover tests were conducted by placing the propeller model outside the wind tunnel test section. Propeller thrust and torque values measured in hover were used both as reference values when evaluating the performance of the propeller in VRS conditions and to compute the descent ratio (DR).

3.1. Aerodynamic performance analysis

Fig. 5 shows propeller thrust and torque coefficients as a function of the descent ratio, DR, for a fixed tilt angle $\alpha = 0\,\text{deg}$. Test results are shown with error bars obtained as the standard deviation of the four repeated loads measurements for each test point. The aerodynamic coefficients were not corrected for wall interference, as existing theoretical models for evaluating solid wall effects in powered propeller wind tunnel tests are only applicable to conditions where the propeller wake develops a definite slipstream boundary with either tip vortices following smooth helicoidal trajectories and the flow highly periodic, such as in climb, or with the wake structure expanding downstream of the propeller, such as in windmill state condition [14].

The measured thrust and torque coefficients exhibit similar behavior when plotted against the descent ratio. As the rate of descent increases, both coefficients decrease gradually compared to their value in hover condition, and they both reach their minimum value at a descent rate of approximately 0.9. This condition corresponds to the onset of VRS for the propeller. Beyond this point, both thrust and torque coefficients start to increase again, and reach their hover values at a descent rate of about 1.11. Results for both propeller rotational speed values studied are also shown in Fig. 5. C_T curves fall almost exactly one on top of the other over the whole range of DR tested, while a small offset can be observed between C_Q curves. Overall, the influence of propeller rotational speed on propeller aerodynamic performance under descent flight conditions was found to be minimal, as the lowest peak of thrust and torque coefficients was found at a similar descent ratio. The propeller aerodynamics coefficients exhibited the characteristic behavior of a conventional helicopter rotor entering in VRS condition during descent flight. Specifically, the highest performance degradation was measured at a descent ratio close to 1, which corresponded to the flight condition where the descent speed was approximately equal to the induced velocity of the propeller in hover.

The performance degradation due to VRS was quantified by comparing the propeller aerodynamic coefficients measured at the onset of VRS condition with their reference values measured in hover. Table 2 shows the propeller thrust and torque coefficients variations, expressed as a percentage of the hover thrust and torque coefficients, for both rotational speed values analyzed. A thrust reduction of slightly more than 20% was observed for both tested rotational speed values at the onset of VRS (DR_{VRS}). On the other hand, the torque coefficient exhibited a variation of less than 10%, with a marginal difference of approximately 2% between the two investigated rotational speeds.

The effects of propeller disk tilt angle on VRS are shown in Fig. 6 where thrust and torque coefficients are plotted as function of descent ratio DR for two different tilt angles, $\alpha = 0°$ and $10°$. The comparisons show that the effects of tilt angle are fairly small in descent conditions, and limited to moderate descent ratios. The onset of VRS occurs in both cases for a descent ratio $DR_{VRS} = 0.9$, and the corresponding performance loss in terms of both thrust and torque is nearly identical. The

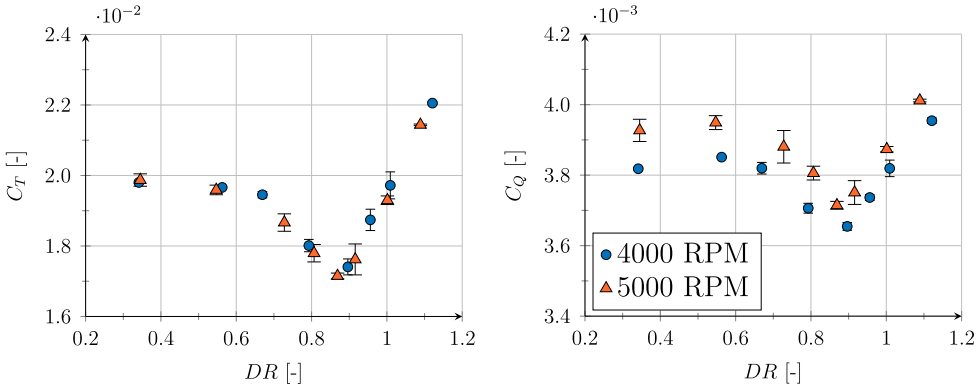


Fig. 5. Propeller thrust and torque coefficients as a function of descent ratio DR at different propeller rotational speeds and tilt angle $\alpha = 0\,\text{deg}$.

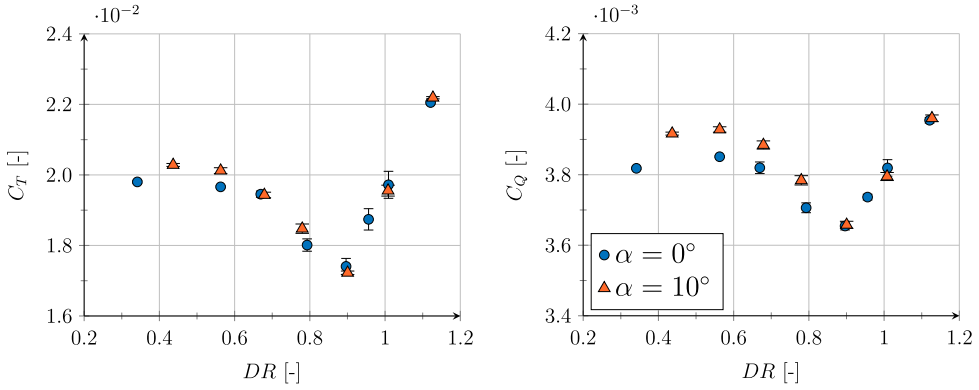


Fig. 6. Propeller thrust and torque coefficients as a function of descent ratio DR, measured with the propeller spinning at a fixed rotational speed of 4000 RPM. Results are shown for two different propeller disk tilt angles (α).

Table 2
Aerodynamic coefficients variations at the onset of VRS. Deltas obtained by comparing the coefficients measured at the descent ratio corresponding to the onset of VRS (DR_{VRS}) and the reference coefficients measured in hover. Results are reported for both propeller rotational speed values tested at a fixed tilt angle $\alpha = 0\,\text{deg}$.

RPM	C_{T_h}	C_{Q_h}	DR_{VRS}	$\Delta C_{T_{VRS}}$	$\Delta C_{Q_{VRS}}$
4000	0.02222	0.00395	0.9	21.7%	7.4%
5000	0.02199	0.00409	0.87	22%	9.4%

effects of propeller disk tilt angle are negligible for descent ratios higher than DR_{VRS} where thrust and torque coefficient curves for different tilt angles almost overlap with each other. For slower descent rates, thrust and torque coefficients values measured at $\alpha = 10°$ are slightly higher than at $\alpha = 0°$, showing a maximum increase of 2.5% and 2.1%, respectively, at $DR \simeq 0.6$.

Finally, a spectral analysis of the load cell signals was performed at the descent ratio corresponding to the onset of VRS (DR_{VRS}). The comparison of the spectra of the thrust and torque signals evaluated for the two rotational speeds and the different tilting angle of the propeller disk is shown in Fig. 7. In particular, the amplitudes of the spectra were normalized with respect to the mean values of thrust and torque measured in the investigated configurations.

The load spectra comparison highlighted the presence of lower frequencies related to the VRS occurrence [15] and enabled to evaluate the differences in terms of peak amplitude for thrust and torque. In particular, a characteristic frequency among 2 Hz was found from the thrust spectra, while torque spectra showed fluctuations amplitude to be quite low, as also found in the literature works by Washizu et al. [16] and presented a peak in correspondence of a slight lower frequency, as also shown by Xin and Gao experiments [17]. Moreover, by considering the spectra comparison for different rotational speeds and tilt angle, a larger amplitude of loads fluctuations associated with VRS onset was found for the higher propeller RPM tested, while comparing the spectra at the same rotational speed, i.e. 4000 RPM, a slight higher peak can be observed at $\alpha = 10°$ with respect to pure axial flight.

3.2. Flow field analysis

PIV measurements conducted on the propeller in descent flight conditions allowed for a detailed examination of the vortex ring formation within the propeller wake. This analysis enabled the observation and tracking of the vortex ring's evolution around the propeller disk as the descent velocity varied. Figs. 8 and 9 show the flow fields averaged over the 300 image pairs measured at 4000 RPM and 5000 RPM respectively for five descent ratio values ranging from 0.7 to 1.1 in increments of 0.1. In particular, when the propeller rotational speed was set to 4000 RPM a series of descent speeds from $V_\infty = 6\,\text{m s}^{-1}$ to $10\,\text{m s}^{-1}$ were tested, while for 5000 RPM the descent speed ranged from $V_\infty = 8\,\text{m s}^{-1}$ to $12\,\text{m s}^{-1}$. Velocity magnitude contours are shown together with the local direction of the flow by in-plane streamlines.

The flow field images provide a clear cross-sectional view of the large vortex characteristic of the VRS phenomenon. As the descent velocity increases, the vortex shifts its position from downstream to upstream of the propeller disk. As expected, the flow fields measured at 4000 and 5000 RPM exhibit similar features when comparing images taken at the same descent ratio. The propeller performance results, quantified by load cell measurements discussed in the previous paragraph, and the flow field characteristics around the propeller disk, visualized through PIV measurements, demonstrated a clear correlation when analyzed at corresponding descent ratios.

For a moderate low descent ratio ($DR = 0.7$, see Figs. 8(a) and 9(a)) two distinct regions, the propeller slipstream and the surrounding recir-

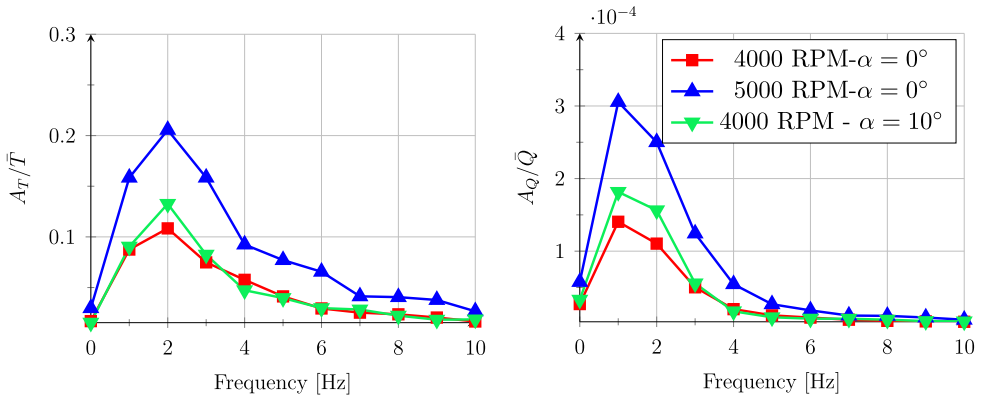


Fig. 7. Comparison of the spectra of the thrust and torque signals at the descent ratio corresponding to the onset of VRS (DR_{VRS}). Results are reported for both propeller rotational speed values tested and both tilt angle, $\alpha = 0$ deg and $\alpha = 10$ deg.

culation area, can be recognized within the PIV interrogation window around the propeller. The propeller slipstream is, as expected, characterized by high velocities when compared to the other regions. In contrast, the areas surrounding the propeller and its slipstream show the onset of a massive recirculating flow structure that results from the interaction of the propeller and the freestream. At this descent ratio, the recirculating flow structure downstream of the propeller disk influences the propeller inflow by reducing the effective angle of attack of the aerodynamic sections along the blade span. In this condition, both measured C_T and C_Q values are lower with respect to the reference values measured in hover condition (see Table 2).

As the descent speed increases, a coherent large vortex structure approaching the propeller blades appears in the PIV investigation area (see Figs. 8(b) and 9(b)). As the magnitude of the descent speed approaches that of the propeller downwash, a well organized large vortical structure reaches the tip of the propeller blades. For a descent ratio $DR_{VRS} = 0.9$ the vortical structure is observed to be well-centered with respect to propeller disk (see Figs. 8(c) and 9(c)). The propeller is now working in VRS condition [1,2], and the flow field around the disk is characterized by a large recirculating flow area producing a robust reduction of local effective angle of attack along the entire blade span. This behavior is responsible for the highest aerodynamic performance loss observed at $DR_{VRS} = 0.9$ for both rotational speeds considered in this study (see Fig. 5).

A further increase in descent speed results in a vortex ring that, while maintaining a degree of coherence, is progressively displaced upstream of the propeller disk (see Figs. 8(d)-8(e) and 9(d)-9(e)). Although the propeller blades remain exposed to the vortex ring while it migrates upstream and away from the propeller disk, the induced effects on local angle of attack along the blade span diminish as the vortex is no longer centered with respect to propeller disk. For descent ratios greater than 1, the freestream velocity surpasses the magnitude of the propeller slipstream velocity. This imbalance forces the propeller into a turbulent wake state [1,2]. In this new state, the propeller experiences a recovery in its aerodynamic performance, as clearly indicated by previous measurements of propeller thrust and torque (see Fig. 5).

PIV measurements with propeller disk tilted by $\alpha = 10°$ were performed at 4000 RPM only for three descent ratios, i.e. $DR = 0.7, 0.9, 1.1$. As can be observed by the averaged flow fields reported in Fig. 10, the outcome of these velocity surveys show the same topology of the VRS operating states observed in pure axial descent flight conditions, except for a radial outward shift of the vortex core with respect to propeller disk.

A quantitative evaluation of the vortex ring position was conducted by calculating the vortex center and radius for the descent ratio corresponding to the VRS condition ($DR_{VRS} = 0.9$). Specifically, the vortex center was determined using an approach based on the identification of the vortex location by tracing in-plane streamlines from the PIV-averaged flow fields. When streamlines twist or close around a circular structure, they provide a clear identification of the vortex core. In particular, the center of curvature method was used in the present work, as described in details in [18]. Indeed, in vortical regions of the flow field, the centers of curvature of several nearly circular streamlines accumulate at a point, that is considered the vortex center position. This method was applied to the averaged flow fields to provide a comprehensive understanding of the vortex ring evolution around the propeller by analyzing the trajectories of the vortex core centers along the entire range of descent ratios for all tested conditions. This analysis enabled the tracing and comparison of vortex ring paths during descent flight. A limitation of the accuracy of vortex ring positioning has to be acknowledged for the test condition at $DR = 0.7$ and 4000 RPM, where the circular structure of the streamline around the vortex center appears not completely closed in the PIV measurements area (see Figs. 8(a) and 10(a)).

Fig. 11 presents a comparison of these trajectories for the two propeller rotational speeds analyzed in pure axial descent flight, as well as for the configuration with the propeller disk tilted by an angle $\alpha = 10°$ at 4000 RPM. As expected, in pure axial descent flight conditions ($\alpha = 0°$) the vortex ring cores move along the same trajectory regardless of the propeller rotational speed setting, showing minor differences for a given location along their path. This result proves that the spatial evolution of the vortex ring is largely independent of the propeller's rotational speed. Non-negligible differences can be observed by comparing vortex cores trajectories for a given propeller rotational speed (i.e. 4000 RPM) and different propeller disk tilt angles. Vortex trajectory analysis enabled to quantify how much the vortex core measured with the propeller disk tilted by an angle $\alpha = 10°$ is radially shifted outward from propeller disk with respect to the vortex core measured in pure axial descent flight condition. In particular, by rotating the propeller disk by 10° with respect to the freestream, the vortex ring core at $DR_{VRS} = 0.9$ is pushed away from propeller disk by about $15\%R$ with respect to the axial descent flight condition. The magnitude of the radial shift observed is comparable with the magnitude by which the vortex ring radius increases when the propeller disk is rotated with respect to the freestream (see Table 3). The radial shift of the vortex is compensated by an increase in vortex radius. Consequently, the vortex ring, which induces variations in the local angle of attack along the blade span through its recirculating flow, alters the propeller inflow in a manner similar to that observed in pure axial descent flight. The interplay between these two opposing effects explains the comparable aerodynamic performance losses observed at 4000 RPM for both $\alpha = 0°$ and $\alpha = 10°$.

The analysis of PIV time-averaged flow field cannot provide accurate insights about the evaluation of vortex ring dimensions. Indeed, the vortex core is characterized by a random low-frequency oscillation associated with the unsteady nature of the VRS phenomenon, commonly referred to as vortex meandering or wandering in rotor blade tip vortices

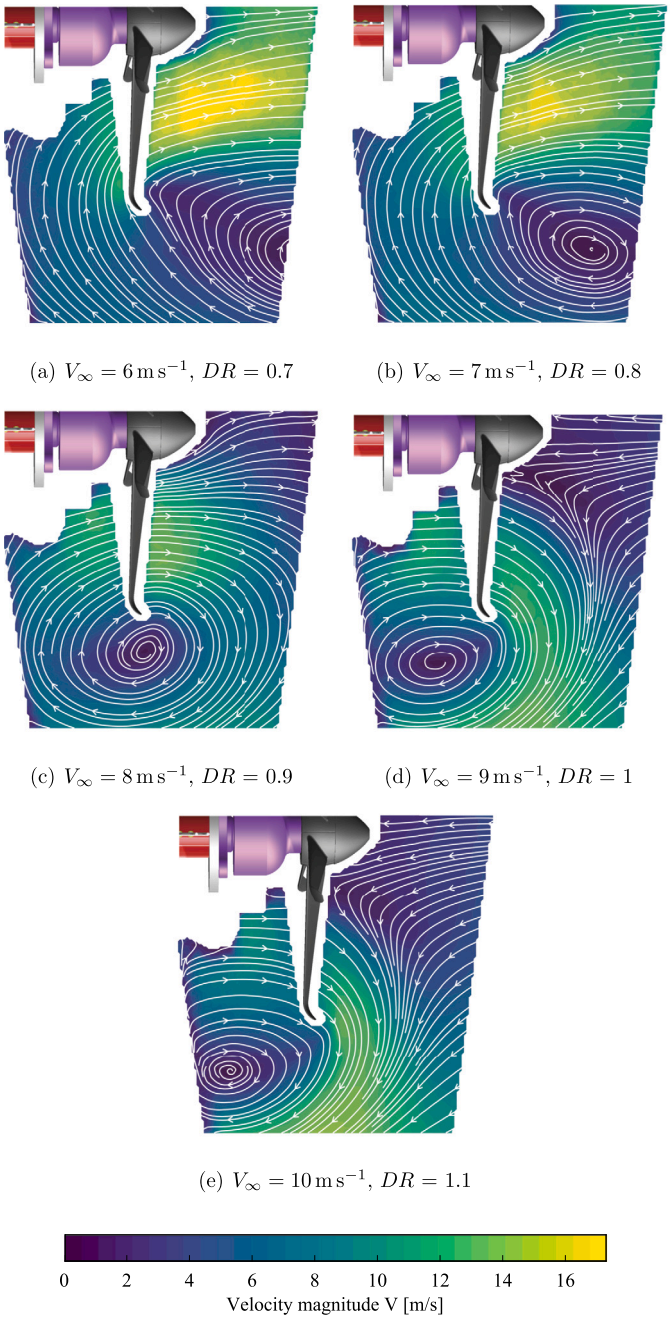


Fig. 8. 2D PIV mean flow fields around the propeller in descent conditions at 4000 RPM and 0° tilt angle. (For interpretation of the colors in the figure(s), the reader is referred to the web version of this article.)

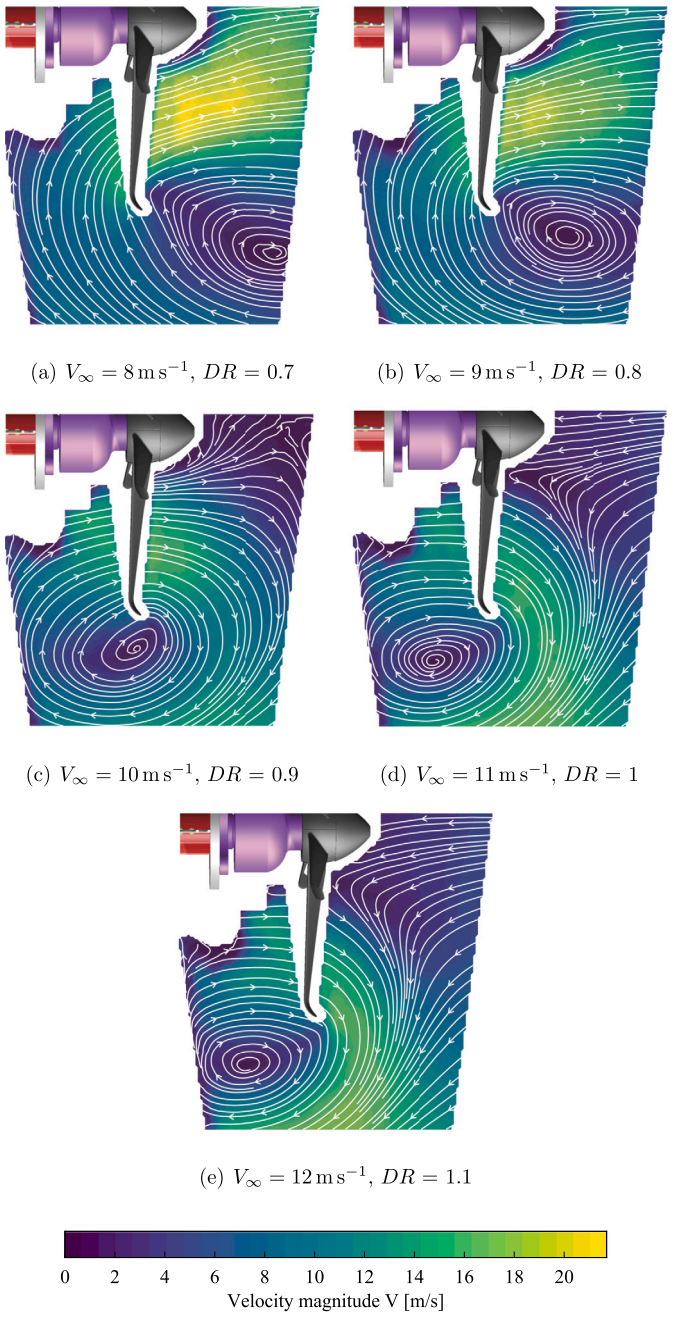


Fig. 9. 2D PIV mean flow fields around the propeller in descent conditions at 5000 RPM and 0° tilt angle.

[19,20]. As noted by Devenport et al. [21], this wandering is responsible of a smoothing effect that can provide an underestimation of the peak tangential and axial velocities from the time average velocity fields and an overestimation of the vortex core diameter. To address this point, Heyes and Smith [22] propose to re-centers the vortex cores calculated from all instantaneous PIV flow fields with the location of the time-averaged vortex center. Thus, the tangential velocity field (V_θ) can be calculated by averaging the re-centered in-plane velocity components. The vortex core radius, r_v, can be then determined as the radial distance from the time-averaged vortex center where the averaged tangential velocity, calculated on the area of investigation, reaches its maximum value (V_{θ_v}), as done in Gibertini et al. [23]. This methodology was applied in the present work to the instantaneous PIV flow fields collected at VRS onset, i.e. $DR_{VRS} = 0.9$, in order to provide comparative results in terms of vortex ring dimensions. However, this analysis encountered some limitations. Indeed, as a matter of fact, the detection of the vortex ring center was ambiguous or not feasible for a certain number of instantaneous flow field images, due to the absence of a clearly visible, well-defined, coherent vortical structure (see Fig. 12(a)) or the presence of multiple vortices with different core dimension inside the interrogation window (see Fig. 12(b)). Thus, the strong unsteadiness of the flow physics outlined by the instantaneous PIV fields would make unfeasible a proper application of wandering correction analysis. Nevertheless, in order to overcome this limitation and provide a reliable comparative evaluation of the vortex ring radius and of the vortex core oscillation amplitude among the investigated conditions, the centers of the vortex cores were determined from flow fields averaged across 10 pairs of PIV images, corresponding to an acquisition time of 1 s. This method resulted in 30 averaged flow fields from the 300 image pairs acquired

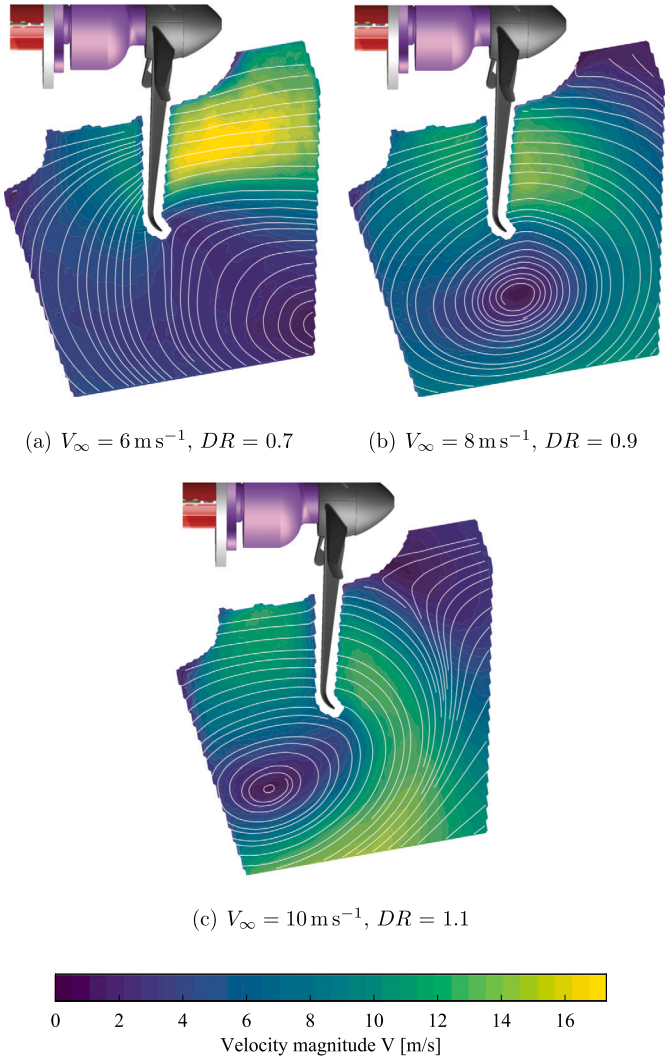


Fig. 10. 2D PIV mean flow fields around the propeller in descent conditions at 4000 RPM and 10° tilt angle.

Table 3
Comparison of the vortex ring characteristics for the descent ratio corresponding to the onset of VRS condition, i.e. $DR_{VRS} = 0.9$.

RPM	α	r_v/R	V_{θ_v} / V_{tip}
4000	0	0.485	0.171
4000	10	0.604	0.178
5000	0	0.490	0.163

during the PIV surveys carried out at a frequency of 10 Hz, that were re-centered on the time-averaged vortex center to evaluate the vortex ring radius and the maximum tangential velocity, as described before.

Table 3 shows the comparison of the calculated values of vortex ring radius and of the maximum tangential velocity at the descent ratio corresponding to the onset of VRS condition ($DR_{VRS} = 0.9$). In particular, the maximum tangential velocity was normalized with respect to the blade tip speed (V_{tip}), in order to take into account the influence of the propeller rotating speed.

The vortex ring radius r_v, computed for the different rotational speeds investigated under pure axial descent flight conditions ($\alpha = 0°$), was nearly identical, approximating in both cases half the propeller blade radius. The normalized maximum tangential velocity V_{θ_v} shows slight variations between 4000 RPM and 5000 RPM, thus indicating a

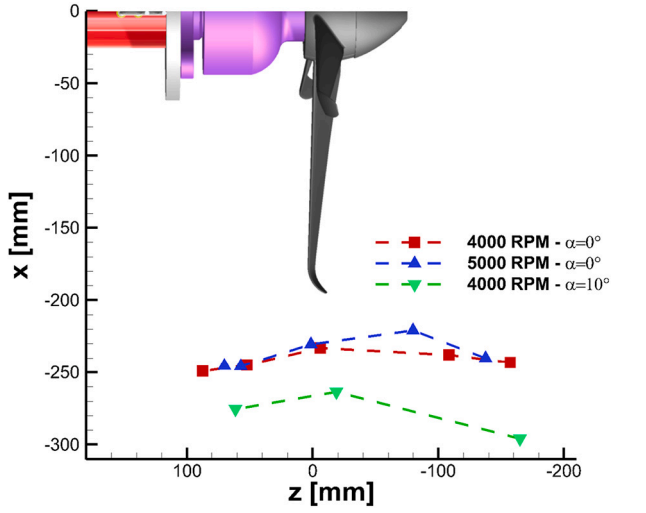


Fig. 11. Comparison of vortex ring center trajectories from the averaged flow fields as a function of the descent rate, $0.7 < DR < 1.1$.

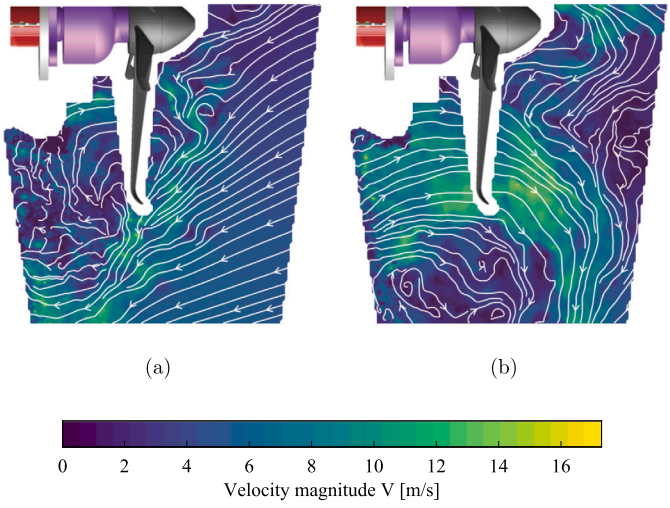
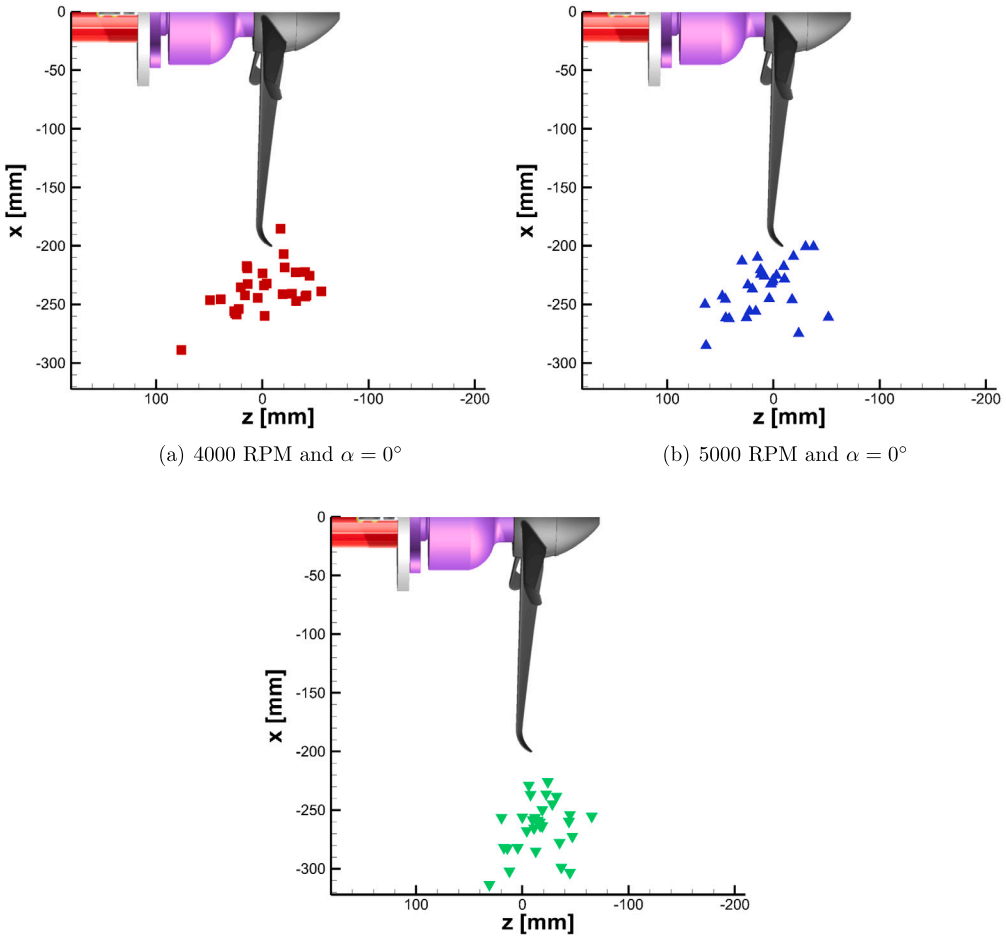


Fig. 12. Sample 2D PIV instantaneous flow fields around the propeller in descent conditions at 4000 RPM, $DR = 0.9$ and 0° tilt angle.

quite low sensitivity in the vortex ring intensity with respect to rotational speeds. Conversely, when the propeller disk was tilted at $\alpha = 10°$, the vortex ring radius is larger with respect to the value obtained in the pure axial descent condition at 4000 RPM (i.e. about 12% of the propeller radius R). Despite the increase in vortex radius, the maximum tangential velocity V_{θ_v} remained nearly constant, indicating that the vortex intensity was largely unaffected by the propeller tilt angle.

Moreover, Fig. 13 compares the distribution of vortex centers positions obtained averaging instantaneous pairs of PIV images over 1 s of acquisition time at $DR_{VRS} = 0.9$ for different propeller rotational speeds and with both the propeller disk perpendicular to the freestream and rotated of an angle of 10°. Additionally, the standard deviation of the vortex ring center positions along the x- and z-axes are presented in Table 4 to provide a comparative measure of the entity of the vortex wandering amplitude.

The standard deviations of the vortex ring center positions along the both $x-$ and $z-$ axes were similar for the tests conducted at the same propeller rotational speed (4000 RPM) with disk angles of $\alpha = 0°$ and $\alpha = 10°$. This result suggests that the vortex wandering is insensitive to relatively small changes in disk orientation (tilt angle) with respect to the freestream when the propeller is operating in descent flight conditions. Furthermore, the vortex wandering along $x-$ and z-axis directions



(a) 4000 RPM and $\alpha = 0°$ (b) 5000 RPM and $\alpha = 0°$

(c) 4000 RPM and $\alpha = 10°$

Fig. 13. Distribution of the vortex ring center positions obtained averaging instantaneous pairs of PIV images over 1 s of acquisition time.

Table 4
Standard deviation of the vortex ring center position along $x-$ and $z-$ axis for descent ratio corresponding to the onset of VRS condition, i.e. $DR_{VRS} = 0.9$.

RPM	α	σ_{v_x} [mm]	σ_{v_z} [mm]
4000	0	19.5	31.1
4000	10	21.4	28.5
5000	0	22.2	22.4

is equal, respectively, to about 10% and 15% of the propeller blade radius. Present vortex wandering results for a propeller in descent flight conditions appear to be substantially different from that observed by Karpatne et al. [24] who investigated the wandering motion of tip vortices trailing from a hovering helicopter rotor and estimated the axial and radial range of tip vortices drift to be approximately between 5% to 10% of the blade chord length. The comparison of standard deviation values in pure axial descent flight at different rotational speeds reveals a similar magnitude of vortex ring center wandering along the x-axis direction. However, at the higher rotational speed (5000 RPM), the vortex ring center positions exhibit comparable wandering along both Cartesian directions, with a notably lower standard deviation along the z-axis compared to the test at 4000 RPM.

4. Conclusions

This experimental investigation re-examined the vortex ring state phenomenon in the context of eVTOL propeller applications in descent flight conditions. Wind tunnel tests were conducted to assess the effects of this critical aerodynamic phenomenon on propeller performance, both in pure axial descent flight (i.e. with the propeller disk normal to the freestream) and with the propeller disk rotated by a small angle with respect to the freestream. The latter condition provided novel insights into VRS behavior under flight conditions specific to eVTOL designs. Additionally, PIV measurements facilitated a detailed analysis of the flow physics associated with VRS onset and evolution in relation to the descent ratio, defined as the ratio between the freestream velocity and the induced velocity of the propeller in hover.

Propeller performance were acquired through a bi-axial load cell. Propeller thrust and torque measurements showed that the onset of VRS condition consistently occurred at the same descent ratio ($DR_{VRS} = 0.9$) across all tested rotational speeds (4000 and 5000 RPM). Furthermore, a substantial performance degradation was observed at the onset of VRS condition as both thrust and torque coefficients dropped, respectively, by about 20% and 10%, when compared to hover. The introduction of a small propeller disk tilt angle did not produce any relevant differences both in terms of descent ratio corresponding to the onset of VRS and the magnitude of the observed performance losses. Moreover, the spectral analysis of the load cell signals enabled to identify the characteristics lower frequencies related to the VRS occurrence and enabled to evaluate the differences in terms of loads oscillations amplitude related to the unsteadiness of the phenomenon with respect to the propeller rotational speed and tilting angle.

The analysis of the averaged flow fields provided a precise characterization of the physical phenomena observed during the descent of a propeller, including slow descent, vortex ring state, and turbulent wake state. A quantitative analysis of the tangential velocity field enabled

a quantitative comparison of the vortex ring features. Propeller rotational speed did not significantly impact the vortex's ring dimensions. However, a higher propeller rotational speed resulted in more intense vortices at a given descent ratio. When the propeller disk was tilted at a non-zero angle with respect to the freestream, the vortex ring exhibited increased dimensions and a radial shift of its core compared to pure axial descent flight conditions. An analysis of the instantaneous flow fields revealed insights into vortex ring wandering. The results suggest a minimal dependence of vortex core fluctuations on propeller rotational speed and negligible effects for a small tilt angle of the propeller disk.

Overall, the experimental data set generated through this study offers valuable insights into the re-evaluation of the VRS phenomenon for an eVTOL propeller in descent flight. This study also provides a comprehensive set of data that can be used for numerical tools validation activities. Numerical tools are crucial for investigating the effects of complex phenomena, such as VRS, on eVTOL vehicles. For instance, in the case of VRS, they can assist designers in predicting the behavior of the aircraft as it approaches VRS conditions and in developing control strategies to avoid entering, or escape, VRS conditions. However, it is important to remember that such numerical tools need to be extensively validated via experiments (either wind tunnel or flight test) in order to be considered reliable. This experimental validation is a critical step in ensuring the accuracy and trustworthiness of the simulations. The use of a scaled model representative of the *Maker* eVTOL tilter propeller provided by Archer Aviation, a leading eVTOL industry partner, ensures that the experimental data presented in this paper can serve as a robust basis for validating numerical tools used for both vehicle design and aircraft performance prediction.

CRediT authorship contribution statement

Alberto Savino: Writing – original draft, Visualization, Validation, Software, Methodology, Investigation, Formal analysis, Data curation, Conceptualization. **Andrea Gianotti:** Writing – original draft, Visualization, Software, Methodology, Investigation, Formal analysis, Data curation. **Giovanni Droandi:** Writing – review & editing, Supervision, Resources, Project administration, Investigation, Funding acquisition, Formal analysis, Conceptualization. **Mike Kerho:** Writing – review & editing, Supervision, Software, Project administration, Investigation, Funding acquisition, Conceptualization. **Alex Zanotti:** Writing – review & editing, Writing – original draft, Validation, Supervision, Resources, Project administration, Investigation, Funding acquisition, Formal analysis, Data curation, Conceptualization.

Declaration of competing interest

The authors declare that they have no known competing financial interests or personal relationships that could have appeared to influence the work reported in this paper.

Acknowledgements

This research was performed by using staff and facilities of the Aerodynamics Laboratory of the Department of Aerospace Science and Technology of Politecnico di Milano. Authors would acknowledge Donato Grassi and Luca Riccobene from Politecnico di Milano for their technical support in the set up, development, and wind tunnel tests.

Data availability

Data will be made available on request.

References

[1] G.J. Leishman, Principles of Helicopter Aerodynamics, Cambridge University Press, 2006.
[2] W. Johnson, Rotorcraft Aeromechanics, vol. 36, Cambridge University Press, 2013.
[3] G.D. Padfield, Helicopter Flight Dynamics: Including a Treatment of Tiltrotor Aircraft, John Wiley & Sons, 2018.
[4] K. Mort, P. Yaggy, Wind-tunnel tests of two vtol propellers in descent, Tech. Rep., 1963.
[5] M.D. Betzina, Tiltrotor descent aerodynamics: a small-scale experimental investigation of vortex ring state, in: American Helicopter Society 57th Annual Forum, Washington, DC, 2001.
[6] A. Brand, R. Kisor, R. Blyth, D. Mason, C. Host, V-22 high rate of descent (hrod) test procedures and long record analysis, in: American Helicopter Society 60th Annual Forum, Baltimore, MD, 2004.
[7] J. Stack, Experimental investigation of rotor vortex wakes in descent, in: 42nd AIAA Aerospace Sciences Meeting and Exhibit, 2004, p. 297.
[8] O. Shetty, M. Selig, Small-scale propellers operating in the vortex ring state, in: 49th AIAA Aerospace Sciences Meeting Including the New Horizons Forum and Aerospace Exposition, 2011, p. 1254.
[9] O. Inoue, Y. Hattori, K. Akiyama, O. Inoue, Y. Hattori, K. Akiyama, Calculations of vortex ring states and autorotation in helicopter rotor flow fields, in: 28th Fluid Dynamics Conference, 1997, p. 1847.
[10] M. Şenipek, I.D. Okçu, O. Tekinalp, M.K. Leblebicioğlu, System Identification of e-Vtol Rotor in Vortex Ring State by Viscous Vortex Particle Method, 2023.
[11] J. Lu, Y. Lu, J. Wang, X. Xu, M. Shao, Numerical investigation of the quasi-vortex-ring state of the propulsive wing in vertical descent, Aerosp. Sci. Technol. 132 (2023) 108075, https://doi.org/10.1016/j.ast.2022.108075, https://www.sciencedirect.com/science/article/pii/S1270963822007490.
[12] M. Raffel, C. Willert, S. Wereley, J. Kompenhans, Particle Image Velocimetry — a Practical Guide, Springer, Berlin, 2007.
[13] F. De Gregorio, K. Pengel, K. K, A comprehensive piv measurement campaign on a fully equipped helicopter model, Exp. Fluids 53 (2012) 37–49.
[14] B. Ewald, et al., Wind Tunnel Wall Correction, AGARD, North Atlantic Treaty Organization, 1998.
[15] W. Johnson, Model for vortex ring state influence on rotorcraft flight dynamics, Tech. Rep., 2005.
[16] K. Washizu, A. Azuma, J. Koo, T. Oka, Experiments on a model helicopter rotor operating in the vortex ringstate, J. Aircr. 3 (3) (1966) 225–230.
[17] H. Xin, Z. Gao, An experimental investigation of model rotors operating in vertical descent, in: 19th European Rotorcraft Forum, Cernobbio, Italy, 1993.
[18] I. Ari Sadarjoen, F.H. Post, Detection, quantification, and tracking of vortices using streamline geometry, Comput. Graph. 24 (3) (2000) 333–341, https://doi.org/10.1016/S0097-8493(00)00029-7, https://www.sciencedirect.com/science/article/pii/S0097849300000297.
[19] J.G. Leishman, A. Bagai, Challenges in understanding the vortex dynamics of helicopter rotor wakes, AIAA J. 36 (7) (1998) 1130–1140.
[20] H. Gao, L. Gao, Z. Shi, D. Sun, X. Sun, Reconstruction and prediction of the rotor wake flow field in hovering state, Aerosp. Sci. Technol. 147 (2024) 108977, https://doi.org/10.1016/j.ast.2024.108977, https://www.sciencedirect.com/science/article/pii/S127096382400110X.
[21] W.J. Devenport, M.C. Rife, S.I. Liapis, G.J. Follin, The structure and development of a wing-tip vortex, J. Fluid Mech. 312 (1996) 67–106, https://doi.org/10.1017/S0022112096001929.
[22] A. Heyes, D. Smith, Spatial perturbation of a wing-tip vortex using pulsed span-wise jets, Exp. Fluids 37 (2004) 120–127.
[23] G. Gibertini, A. Mencarelli, A. Zanotti, Oscillating aerofoil and perpendicular vortex interaction, Proc. Inst. Mech. Eng., G J. Aerosp. Eng. 228 (6) (2014) 846–858, https://doi.org/10.1177/0954410013481154.
[24] A. Karpatne, J. Sirohi, S. Mula, C. Tinney, Vortex ring model of tip vortex aperiodicity in a hovering helicopter rotor, J. Fluids Eng. 136 (7) (2014) 071104.